Journal Pre-proof

Nanoscale Fe-Containing Intermetallic Formation in Al-Fe-Mn-Si Alloys: Unveiling a Rare Explosive Nucleation Pathway under Liquid Confinement

Zhongping Que, Raluca Florentina Negrea, Zhongyun Fan

PII: S2352-4928(26)00098-X

DOI: https://doi.org/10.1016/j.mtcomm.2026.114714

Reference: MTCOMM114714

To appear in: *Materials Today Communications*

Received date: 3 November 2025
Revised date: 15 January 2026
Accepted date: 20 January 2026

Please cite this article as: Zhongping Que, Raluca Florentina Negrea and Zhongyun Fan, Nanoscale Fe-Containing Intermetallic Formation in Al-Fe-Mn-Si Alloys: Unveiling a Rare Explosive Nucleation Pathway under Liquid Confinement, *Materials Today Communications,* (2026) doi:https://doi.org/10.1016/j.mtcomm.2026.114714

Nanoscale Fe-Containing Intermetallic Formation in Al-Fe-Mn-Si Alloys: Unveiling a Rare Explosive Nucleation Pathway under Liquid Confinement

Zhongping Que*, Raluca Florentina Negrea, Zhongyun Fan

Brunel Centre for Advanced Solidification Technology (BCAST), Brunel University London, Uxbridge, Middlesex UB8 3PH, UK

*Corresponding author. Tel.: +44 1895 268535; E-mail address: Zhongping.Que@brunel.ac.uk

Abstract:

Iron (Fe) is an unavoidable impurity in recycled aluminium (Al), where the formation of Fe-containing intermetallic compounds (Fe-IMCs) severely reduces ductility and performance due to their coarse morphology. The nucleation difficulty of Fe-IMCs remains a critical barrier to both Fe removal efficiency and refinement of Fe-IMCs as secondary phases, limiting the use of recycled feedstock in high-performance applications. Conventional approaches have focused on development potent grain refiners to promote heterogeneous nucleation by providing structural and compositional templating. However, despite advances in nucleation theory and refiner development, significant refinement of Fe-IMCs has proven elusive. In this study, we report an unexpected case of impeding heterogeneous nucleation, where nanoscale Fe-IMCs explosively form within confined oxide films in an Al-Fe-Mn-Si alloy. Using advanced scanning transmission electron microscopy (STEM) we reveal that dense amorphous oxide films and carbides act as substrates for impeding nucleation. These results highlight how that confinement oxide films can activate non-classical nucleation pathways, offering the other possibility to control Fe-IMC formation and enhance the upcycling potential of recycled Al alloys.

Keywords: Oxide films, heterogeneous nucleation, amorphous oxides, Fe-containing intermetallic compounds, Si

1. Introduction

In pursuit of a sustainable, net-zero future, efficient circulation of metals is critical for minimizing environmental impact and conserving natural resources. Among industrial metals, aluminium stands out due to its excellent recyclability, with recycled production consuming only ~5-10% of the energy required for primary production [1-3]. As global demand for aluminium continues to rise, particularly in automotive, aerospace, and packaging sectors, recycling of Al alloys becomes increasingly vital for achieving sustainability goal. Despite these advantages, recycling faces significant challenges, especially in managing impurities. Among them, iron (Fe) is one of the unavoidable impurities and represents the most critical issue [4-9]. Due to its low solubility in aluminium and its tendency to form coarse Fe-containing intermetallic compounds (Fe-IMCs) at high temperature, Fe significantly degrades

mechanical properties, particularly ductility. This limitation restricts the transition from primary to secondary aluminium resources and poses a major challenge for producing high-performance recycled alloys.

Over the past decades, two main approaches have been explored to address Fe-related challenges in recycled aluminium. The first approach aims to remove excess Fe by accelerating the nucleation of Fe-IMCs, attempting to overcome the current Fe removal limit of ~0.7 wt.% [8-9]. The second approach focuses on refinement of Fe-IMCs through techniques such as alloying additions (e.g., Mn, Cr) to modify morphology [10-11], grain refinement [12], or physical treatments such as high-shear stirring [13]. While these methods have achieved some success, they remain inherently limited by difficulties in controlling nucleation and growth of Fe-rich phases, due to an incomplete understanding of their formation mechanisms. Consequently, deeper insight into the evolution, distribution, and behaviour of Fe-containing phases in recycled aluminium alloys is essential for advancing alloy design and processing strategies.

Recent years, the formation mechanisms of Fe-IMCs in aluminium alloys have been extensively investigated [14-17]. Systematic studies reveal that the unpredictable formation behaviour of Fe-IMCs often deviating from equilibrium phase diagram prediction, which is primarily due to nucleation difficulties arising from complex phase selection competitions during solidification, followed by intricate transformation pathways. Although the existence of Fe-IMCs in aluminium alloys was firstly recognized nearly a century ago [18-20], effective and scalable solutions remain elusive. To date, reliably reducing Fe content below 0.3 wt.% or refining secondary Fe-IMC particle sizes to nanometre scale continues to be extremely challenging. The lack of fundamental understanding of nucleation and growth mechanisms, particularly under non-equilibrium processing conditions, hinders the development of efficient removal and/or refinement strategies.

Earlier studies under conventional casting conditions demonstrated that the nucleation of Fe-IMCs requires both structural and compositional templating [12], highlighting the intrinsic difficulty of their formation compared with single-phase nucleation such as α-Al. More recently, the impeding nucleation theory has proposed a novel approach to achieve significant grain refinement by increasing nucleation undercooling using impotent nucleation particles [21]. Achieving explosive nucleation has long been regarded as a breakthrough strategy for refining Fe-IMCs, particularly in controlling the nucleation of primary phases. Such a mechanism would not only reduce Fe levels to ultra-low concentrations but also enable the refinement of secondary Fe-rich phases.

In this study, we report a significant refinement of Fe-IMCs to the nanoscale via explosive heterogeneous nucleation occurring within confined melt regions encapsulated by oxide films in an Al-Fe-Mn-Si alloy. The underlying mechanism and nucleation characteristics were investigated using advanced scanning transmission electron microscopy (STEM), which revealed features consistent with the impeding nucleation pathway. These findings are critical for advancing technologies aimed at refining Fe-intermetallic compounds in recycled

aluminium alloys and reveal a promising pathway for inducing explosive nucleation of Fe-IMCs to address the Fe challenge in high-performance recycled aluminium. Although this study reports only an isolated case of nanoscale Fe-IMC refinement, it nevertheless demonstrates the feasibility of nucleation-controlled strategies and provides a foundation for developing practical technologies.

2. Experimental

2.1 Casting

The alloy investigated in this study had a composition of 0.92 ± 0.3 wt.% Mn, 2.26 ± 0.3 wt.% Fe, and 4.85 ± 0.5 wt.% Si, with the balance being Al. The composition was measured using a Foundry Master spectrometer. The solidification sequence of this studied alloy was calculated with Pandat software under the Sheil model [22] as follows: L→ α-$Al_{15}(Fe,Mn)_3Si_2$ (P-IMC), L → α-$Al_{15}(Fe,Mn)_3Si_2$ (BE-IMC) + α-Al, L→ α-$Al_{15}(Fe,Mn)_3Si_2$ (TE-IMC) + α-Al + α-Al_8Fe_2Si, L→ α-$Al_{15}(Fe,Mn)_3Si_2$ (TE-IMC) + α-Al + β-Al_5FeSi and L→ α-$Al_{15}(Fe,Mn)_3Si_2$ (TE-IMC) + Si + β-Al_5FeSi. The calculated melting temperature of the alloy was 694 °C. Commercially pure (CP) Al (>99.8 wt.%) and master alloys of Al-50 wt.% Si, Al-20 wt.% Mn, and Al-38 wt.% Fe were used for the casting. The CP-Al and all the master alloys were firstly melted at 750 °C in an electric resistance furnace. Subsequently, the molten aluminium was thoroughly stirred for approximately 1 hour to ensure complete dissolution of master alloys. The melt was then held for an additional 30 minutes to promote homogeneity. After slag removal, the melt was poured into a TP-1 mould [23], which had been preheated to 380 °C. The TP-1 mould is specifically designed to produce a cooling rate of approximately 3.5 K/s at a sample section located 38 mm from the bottom, comparable to that of directional chill casting. The pouring temperature was maintained at 750 °C.

To investigate the role of oxides in the heterogeneous nucleation of Fe-IMCs, a pressurized melt filtration technique was employed. Approximately 2 kg of melt at 800 °C was transferred into a preheated filtration crucible equipped with a ceramic filter with a 40 μm mesh positioned at the bottom. Argon gas was applied at a pressure of 58 psi (~4bar) to force the molten metal through the filter while simultaneously isolating it from atmospheric exposure. The filtered melt was collected, reheated to 750 °C, and subsequently cast into a TP-1 mould. The filtered sample was sectioned for SEM and TEM analyses. The ceramic filter was removed to avoid cutting difficulties, and the specimen was then cut along the longitudinal midline corresponding to the filter position. After estimating the thickness of the oxide accumulation region, sample was taken approximately 3-4 cm above the filter. The longitudinal section, extending from the filter position to several centimetres above it, was mounted and polished for SEM observation. A thin slice (~1 mm thick) taken just above the filter within the oxide accumulation region was sectioned for TEM examination. Further details of the filtration method can be found in Ref. [24].

Oxide retention was assessed by examining the distribution and morphology of oxide films and inclusions in the solidified alloy above the filter. Optical microscopy and scanning electron microscopy (SEM) were used to identify oxide-rich region, while image analysis was employed

to quantify the area fraction and thickness of the retained oxides. In addition, energy-dispersive X-ray spectroscopy (EDS) was used to confirm the chemical composition. The assessment focused on regions above the filter and within confined melt pockets to capture oxides trapped during solidification.

2.2 Characterization

Metallographic specimens were prepared using standard metallographic procedures. The as-cast microstructural features of the samples were examined using a Zeiss optical microscope equipped with AxioVision 4.3 image analysis software. Scanning electron microscopy (SEM) was conducted using a Zeiss Crossbeam 340 FIB-SEM, operated at accelerating voltages ranging from 5 to 20 kV. To investigate the formation mechanism of nanoscale Fe-IMCs within oxide films, transmission electron microscopy (TEM) specimen was prepared using focused ion beam (FIB) milling on the same Zeiss Crossbeam 340 system. TEM observation was performed using both a Talos F200i and Spectra 300 (Thermo Fisher), operated at 200 kV and equipped with EDS detectors. The crystal structure of the Fe-IMCs was generated using *CrystalMaker* (version 10.8.0) and STEM image simulations were performed using *Tempas* software.

3. Results

3.1 Nucleation difficulty of Fe-IMCs

The Al-1.0Mn-2.2Fe-5Si alloy, both before and after pressurized filtration, was cast at 750 °C under a controlled cooling rate of 3.5 K/s. The resulting microstructures were examined and presented in Fig. 1. Fig. 1a shows the microstructure prior to filtration, revealing several large primary dendritic Fe-IMCs, later identified as α-$Al_{15}(Fe,Mn)_3Si_2$ using SEM-EDS and TEM analysis. These Fe-IMCs exhibit sizes of several hundred micrometres. A higher magnification image, shown in Fig. 1b, reveals that the microstructure consists of three main structures: (i) primary Fe-IMCs, (ii) a binary eutectic structure of Fe-IMCs and α-Al, and (iii) a ternary eutectic composed of Fe-IMCs, α-Al, and Si. The volume fraction of the large primary Fe-IMCs particles was measured to be 9.8±0.5% and their number density was determined as 4.3 x 10^{-5} μm^{-2}.

Fig. 1c shows the microstructure of the alloy solidified at 3.5 K/s cast with after pressurized filtration melt, revealing a noticeable reduction in the number of primary Fe-IMCs and a significant increase in the volume fraction of coarse binary eutectic Fe-IMCs. This observation indicates the role of native oxides and inclusions in the nucleation of primary Fe-IMCs. The volume fraction of the large primary Fe-IMCs particles was measured to be 2.6±0.2% and their number density was determined as 8.5 x 10^{-6} μm^{-2}.

Fig. 1d presents the microstructure of the original alloy solidified at a slow cooling rate of 0.01 K/s. Under this condition, compact primary Fe-IMC particles are observed to have settled,

and several long, dark lines, identified as oxide films with SEM later, are seen intersecting or surrounding the Fe-IMC particles, indicating the nucleation of Fe-IMCs on these oxide films.

3.2 The nano-sized Fe-IMCs

Fig. 2a presents an SEM image of the Al-1.0Mn-2.2Fe-5Si alloy solidified from the melt located above the filter following pressurized filtration. The grey particles, later identified by SEM-EDS as AlFeMnSi IMCs, exhibit a distinct size gradient, increasing in size with distance from the filter. Their morphology evolves from compact to dendritic as size increases, indicating a change in solidification conditions along the vertical section. The compositions of the Fe-IMC particles in the TP-1 and prefilled samples are nearly identical, as confirmed by SEM–EDS analysis (Table 1).

Fig. 2b shows an SEM inlensDuo image of the accumulation of oxides and inclusions in the melt above the filter. The concentration of these collected inclusions decreases with distance from the filter, up to 1 mm in this study. The oxide films appear to be embedded in or associated with Si particles (black) and Fe-rich IMCs (grey). Fig. 2c displays a higher-magnification SEM in-lens image, revealing that the inclusions within the oxide films consist primarily of Al_2O_3 particles (white), along with some carbides (dark grey), indicating the complex nature of the non-metallic inclusions retained in the melt.

An abnormal region approximately 300 μm in diameter, densely populated with nanoscale particles, was observed at about 600-1000 μm above the filter, as shown in Fig. 2d. Fig. 2e reveals that this nanoparticle-rich area is sharply delineated from the surrounding matrix, indicating a distinct boundary. Within this region, the nanoparticles contain embedded oxides (white) and numerous Fe-IMCs (grey). Most of these Fe-IMCs range from 50 to 300 nm in size, although a few particles reach up to approximately 1 μm. High-resolution SEM imaging, shown in Fig. 2f, further reveals the presence of even finer black particles, less than 10 nm in size, distributed throughout the nanoparticle-rich area and frequently associated with or embedded within the Fe-IMCs. These Fe-IMCs particles were measured to have a volume fraction of 22.681% and a number density of about 3.5 μm^{-2}, which showing an explosively increase in number density compared to the TP1 samples before filtration (Fig. 1a 4.3 x 10^{-5} μm^{-2}) and after filtration (Fig.1c, 8.5 x 10^{-6} μm^{-2}).

A FIB lamella was extracted from the nanoparticle-rich region and examined using STEM. Fig. 3a presents a high angle annular dark field (HAADF)-STEM image of the FIB lamella, showing Fe-IMC particles with compact morphologies and sizes ranging from several tens to several hundred nanometres. Numerous fibre-like films are distributed throughout the aluminium matrix and are also present within the Fe-IMCs. STEM-EDS elemental mapping, based on Fig. 3b, is shown in Figs. 3c-i, revealing that the brighter/grey particles are composed primarily of Al, Fe, Mn, and Si. Additionally, Si phases are observed to be associated with these Fe-IMCs particles, while the matrix contains Al, C, N and O, suggesting the presence of embedded oxide and carbide films. The chemical composition of these Fe-IMCs, listed in Table 1, consists of

approximately 70.8 wt.% Al, 14.79 wt.% Fe, 5.56 wt.% Mn, and 8.81 wt.% Si. These measured compositions fall within the reported range for α-$Al_{15}(Fe,Mn)_3Si_2$, as previously documented [14, 15]. The observed differences in Fe-IMC compositions between the bulk, which contains higher Fe, and the TP-1 samples are likely influenced by spatial confinement.

Fig. 4a presents a HAADF-STEM image of a representative Fe-IMC particle, revealing local defects and structural heterogeneity within the particle, suggesting the potential for phase transformation. These features underscore the challenge in determining the crystal structure of such Fe-IMCs. However, clearer structural feature was observed in cleaner and relatively larger particles, enabling identification of the phase as α-$Al_{15}(Fe,Mn)_3Si_2$, as shown in Fig. 4b.

A simulated HAADF-STEM image based on the crystal structure of $Al_{17.1}Fe_{3.2}Mn_{0.8}Si_{1.9}$, obtained from the ICSD database (code: 655126) using Crystalkit and Tempas sofware, is shown in Fig. 4d. This structure belongs to the cubic phase with space group *Im-3* (No.204) and a lattice parameter of $a = 12.56$ Å. The corresponding atomic model, viewed along the [1 0 0] zone axis, is illustrated in Fig. 4e. The parameters used for the HAADF-STEM image simulations were: accelerating voltage of 200 kV, spherical aberration coefficient $C_s = 0.06$ mm, convergence semi-angle of 30 mrad, defocus spread $\Delta f = 20$nm, HAADF detector collection angles (inner–outer) $\beta = 70$–200 mrad, and a sample thickness of $t = 30$nm. The experimental (Fig. 4c) and simulated (Fig. 4d) HAADF-STEM images show good agreement in atomic positions, although some deviations are observed in the Fe/Mn atomic sites when comparing the experimental data with the ideal crystal model. This difference may also arise from variations in elemental concentration.

3.3 Nature of the explosive nucleation

Fig. 5 presents a HAADF image of the Fe-IMCs alongside STEM-EDS elemental maps (Figs. 5b-g), which reveal their association with nanosized Si particles and C and O containing films embedded within the Fe-IMCs. Most Fe-IMC particles are closely associated with oxide or carbide films. The oxides in this confined area differ from those collected above the filter (Fig. 2c), which exhibit large, faceted surface and a regular rectangular or plate-like morphology. In contrast, the oxides within confined area appear to be amorphous in shape. An example of such a structure is illustrated in Fig. 6. The HAADF-STEM image and the corresponding FFT pattern indicate that the attached oxide is amorphous.

Fe-IMC particles in this confined area were occasionally associated with elongated, needle-like dark inclusions as shown in HAADF–STEM image (Fig. 7a). STEM–EDS elemental mapping confirmed that these needle-like structures were enriched in carbon (Fig. 7b–h), which was further verified by the intensity profile (Fig. 7i) extracted along the yellow arrow in Fig. 7a. An HRTEM image of the needle (Fig. 7j) indicated distinct morphological features, although the corresponding FFT pattern did not provide clear evidence of crystallization. Selected-area electron diffraction (SAED) analysis (Fig. 7k), combined with the simulated

SAED pattern of α-$Al_{15}(Fe,Mn)_3Si_2$ along the [305] zone axis (Fig. 7l), enabled identification of the Fe-IMC structure. The overlap of the experimental and simulated SAED patterns (Fig. 7m) confirmed that the Fe-IMC particle was structurally consistent with α-$Al_{15}(Fe,Mn)_3Si_2$ and was closely associated with the adjacent carbon-rich inclusion.

3.4 Silicon nanoparticles

In addition to the formation of nanoscale Fe-IMCs, the Si phase, also reported to be difficult to refine, was observed in this study to undergo significant refinement to the nanoscale. As shown in Fig. 8a, Si particles are consistently associated with Fe-IMCs, but their sizes are notably smaller, typically in the range of 10–100 nm. Atomic resolution STEM observations revealed that these Si particles exhibit pronounced twinning features along the {111} planes, as confirmed by the indexed FFT pattern in Fig. 8d. A distinct core region was observed at the centre of some Si particles (Fig. 8c), appearing crystallography different from the surrounding regions. However, filtered FFT images (Fig. 8e–h) demonstrated that this apparent core does not represent a separate Si phase or an independent nucleation particle. Instead, it corresponds to the overlap of multiple twinning planes converging at the particle centre.

4. Discussion

4.1 Conditions for explosive nucleation of Fe-IMCs in confined oxide films

This study reveals a novel phenomenon: explosive heterogeneous nucleation of Fe-IMCs within confined melt regions encapsulated by oxide films in an Al-2.2Fe-1.0Mn-5.0Si alloy. This isolated microenvironment promotes the formation of a high density of nanosized Fe-IMCs, deviating markedly from the conventional solidification behaviour of Al alloys.

A schematic diagram illustrating the formation of oxide films and their role in trapping liquid, leading to the formation of localized, confined bulk melt regions is shown in Fig. 9. Liquid aluminium instantly forms a thin oxides film (mainly Al_2O_3 and Al_4C_3 in this study due to Mg free) on its surface when exposed to air. During melt processing such as stirring and mixing, the surface agitation causes the film to fold into the melt, it can enclose small amounts of liquid or gas. Once these confined oxide films are stirred into the melt, the small liquid pockets became isolated from the surrounding oxides, preventing further oxidation and growth of oxides or inclusions. These oxide-bounded cavities create confined regions with distinct local chemistry and cooling conditions, which can promote explosive nucleation of Fe-containing intermetallic compounds.

This confinement can drastically reduce atomic exchanges between the confined area and the melt, hinder solute homogenization and cause local enrichment of Fe, Mn, and Si. Consequently, these regions become highly supersaturated with alloying elements during the solidification process, providing favourable conditions for rapid and localized nucleation of Fe-IMCs.

Within these oxide films, numerous nanosized inclusions, including carbon-rich particles, amorphous oxides, become the only available heterogeneous nucleation sites. According to the pre-nucleation theory [24], such particles are considered as impotent nucleation sites due to lack of structural templating which requires large undercooling and higher energy barrier, thereby delayed the nucleation. In contrast, the explosive nucleation theory suggests that, once sufficient undercooling achieved, impeding nucleation can occur explosively in a very short timescale.

After nucleation, the growth of Fe-IMCs is restricted by the physical confinement of the oxide films and the limited fluidity of the enclosed melt. This constrained environment promotes the formation of a high density of ultrafine Fe-IMC particles, in contrast to the few coarse particles typically observed in conventional casting processes (Fig. 1).

4.2 Conditions for Fe-IMCs nucleation on amorphous particles

According to nucleation theory [12, 25-27], under conventional casting conditions, heterogeneous nucleation requires three key factors: sufficient undercooling to thermodynamically drive the process, structural templating to provide crystallographic compatibility, and compositional templating to ensure the appropriate chemical environment. For complex intermetallic compounds such as Fe-IMCs, nucleation is particularly challenging because it demands both precise structural and compositional matching, in addition to significant undercooling [12]. For example, the nucleation of α-$Al_{15}(Fe, Mn)_3Si_2$ requires the ordered arrangement of four different atomic species into specific crystallographic sites, a process far more complex than the nucleation of single-phase materials like pure Al.

However, this study revealed explosive nucleation of nanosized Fe-IMCs occurring on amorphous oxides and/or carbides embedded within confined melt regions. Despite lacking a well-defined crystal structure, these inclusions facilitated rapid nucleation, thereby challenging the conventional requirement for strict structural templating in heterogeneous nucleation.

The impeding nucleation theory [21] proposed a case of explosive nucleation, which particles in the melt are impotent for heterogeneous nucleation, that is, none of them act as effective nucleation sites at low undercooling, so nucleation is delayed until higher degree of undercooling is achieved. At that point, heterogeneous nucleation occurs almost simultaneously at most particles, leading to an “explosive” onset of nucleation and, consequently, significant grain refinement.

The experimental results reported here are consistent with this description of impeding nucleation, as the following conditions are satisfied:

(1) A high density of particles is present. Within the confined oxide films, the oxide density is significantly higher than in the conventional melt, and the oxide particles are uniformly nanoscale and rarely crystalline. This minimizes the influence of size effects on nucleation [27]. Therefore, the explosive nucleation of Fe-IMCs observed in this study represents a

case in which nucleation occurs without structural templating but is instead driven by strong compositional templating combined with an impeding nucleation process.

(2) All nucleation particles are structurally impotent (no effective crystallographic templating is provided). Although amorphous oxides and carbides do not act as ideal structural templates for Fe-IMCs, their surfaces often exhibit strong chemical affinities for alloying elements such as Fe and Mn. Oxygen and other elements within these substrates can chemically interact with solute atoms, promoting the formation of enriched zones adjacent to the particle surface. These enriched zones serve as nucleation precursors and can partially compensate for the absence of crystallographic matching. The heterogeneous nucleation occurring on such particles is analogous to that observed on rough surfaces [28], where defects, steps, and grooves lower free-energy barrier for nucleation. Surface roughness can also modify the effective wetting behaviour of the liquid, further facilitating nucleation. A similar phenomenon is well known in ice nucleation, where dust or mineral particles provide favourable sites for the initiation of ice crystals [29-30].

(3) There is no strong competition from other nucleation sites, such as the casting mould walls or previously crystallized particles. In confined environments, such as liquid trapped within oxide films, typical nucleation substrates, like mould walls, or added grain refiners, are absent or inaccessible. This purification of the local environment reduces the number of effective nucleation sites, delaying nucleation and requiring higher undercooling to initiate. Once this critical undercooling is reached, nucleation occurs explosively, consistent with explosive nucleation theory. The confined space, coupled with limited atomic diffusion, results in localized supersaturation and a steep increase in the thermodynamic driving force for nucleation.

Under these conditions, the formation of significantly refined (nanometre-sized) Fe-IMCs can be interpreted as evidence of explosive nucleation. This supports the validity of the explosive nucleation theory.

4.3 Refinement mechanism of Si

Silicon, despite being a single-element phase, is as difficult to nucleate as Fe-IMCs, requiring a nucleation undercooling of several tens of Kelvin even with phosphorus additions [31]. This nucleation difficulty has been attributed to its crystallographic structure, which imposes a fundamental nucleation barrier, and to its electronic structure and covalent bonding, which further hinder nucleation [32]. In this study, nanoscale Si particles were also observed, in contrast to those formed under conventional casting conditions (Fig. 2b–c), where their sizes are typically on the order of micrometres. However, the nucleation pathway of Si differs from that of Fe-IMCs.

According to the phase diagram, Fe-IMCs solidify prior to Si in the investigated alloy. Consequently, when Si begins to solidify, the remaining melt already contains a high density of nanoscale Fe-IMCs. These pre-existing Fe-IMC particles provide more effective nucleation sites for Si compared with amorphous oxides or carbides. As a result, Si particles are more

likely to nucleate directly on the surfaces of Fe-IMCs. Experimental observation also demonstrated that the majority of Si particles are associated with Fe-IMC particles. This is consistent with the high number density of Fe-IMCs observed in the alloy, with a volume fraction of 22.681% and a number density of about 3.5 μm^{-2}, which substantially enhances the probability of heterogeneous nucleation of Si on Fe-IMC substrates.

4.4 Limitations and future work

The formation of nanoscale Fe-IMCs during solidification is a long-standing goal in addressing the Fe-deterioration problem in recycled Al alloys, yet achieving such refinement has remained extremely challenging. In this work, we reveal a previously unreported explosive nucleation pathway for nanoscale Fe-IMCs triggered by liquid confinement. The resulting microstructures were rigorously characterised using SEM, TEM and STEM techniques, enabling reliable identification of the Fe-IMCs. Nevertheless, this observation is currently based on a limited number of cases and requires further validation.

Future work will incorporate thermodynamic simulations to track solidification-path evolution under different diffusion conditions and to quantify local solute enrichment, thereby enabling more accurate prediction of nucleation behaviour under confined conditions. In addition, a carefully designed experimental system capable of intentionally reproducing such confinement effects will be essential to further explore the mechanism and evaluate its potential for practical application in recycled aluminium processing.

5. Conclusions

In this study, we report a novel observation of explosive heterogeneous nucleation of nano-sized Fe-IMCs within confined melt region enclosed by oxide films in an Al-Fe-Mn-Si alloy. This phenomenon, driven by local thermodynamic and kinetic conditions in the bulk melt, results in the formation of a high density of refined Fe-IMC particles.

1) The confined oxide films formed during casting process act as physical barriers that trap liquid metal, creating localized environments with nanoscale non-crystalline inclusions that promote explosive nucleation of Fe-IMCs.
2) The confined environment not only promotes nucleation but also inhibits subsequent particle growth due to reduced fluidity and limited mass transport. As a result, Fe-IMCs remain nano-sized.
3) The Si phase, which is as difficult to nucleate as Fe-IMCs, was also refined to the nanoscale within this confined melt, nucleating directly on pre-existing Fe-IMCs.

This work advances our understanding of nucleation behaviour in aluminium alloys and offers a new perspective on the role of oxide films. While traditionally considered defects, under specific confined conditions, oxide films can serve as active sites that promote heterogeneous nucleation and influence microstructural evolution. These insights provide a foundation for future melt treatment strategies aimed at controlling Fe-IMCs and improving the performance

and quality of recycled aluminium alloys, while acknowledging that further studies are needed to generalize these findings beyond the specific alloy and local regions examined here.

Funding: This work was financial supported by the EPSRC (UK) under grant number EP/N007638/1 (Future Liquid Metal Engineering Hub) and by Brunel University of London BRIEF award (11937131).
Acknowledgments: We acknowledge the use of the Advanced Characterisation Facility at the Brunel Centre for Advanced Solidification Technology (BCAST), which was established with financial support from Research England UKRPIF 602.

Author Contributions:
Z. Q.: Conceptualization, methodology, experimental investigation, writing, review & editing, funding acquisition.
R. N.: STEM observations & data curation, paper review.
Z. F.: Supervision, funding acquisition.
All authors have read and agreed to the published version of the manuscript.
Conflicts of Interest: The authors declare no conflict of interest.

References

1. International Aluminium Institute publishes global recycling data, www.world-aluminium.org (2024).
2. D. Raabe, D. Ponge, P.J. Uggowitzer, M. Roscher, M. Paolantonio, C. Liu, H. Antreko witsch, E. Kozeschnik, D. Seidmann, B. Gault, F. De Geuser, A. Deschamps, C. Hutchinson, C. Liu, Z. Li, P. Prangnell, J. Robson, P. Shanthraj, S. Vakili, C. Sinclair, L. Bourgeois, S. Pogatscher. Making sustainable aluminum by recycling scrap: the science of "dirty" alloys. Prog. Mater. Sci., 128 (2022) 100947.
3. K.A. Trowell, S. Goroshin, D.L. Frost, J.M. Bergthorson. Aluminum and its role as a recyclable, sustainable carrier of renewable energy. Appl. Energy. 275 (2020) 115112.
4. H.R. Kotadia, N. Bareker, M.H. Khan, J.I. Ahuir-Torres, A. Das. Aluminium recycling: A critical review of iron-bearing intermetallics in aluminium alloys. Materials Today Sustainability, 30, (2025) 101119.
5. N.A. Belov, A.A. Aksenov, D.G. Eskin. Iron in Aluminium Alloys: Impurity and Alloying Element. CRC Press, Taylor & Francis Ltd (2002)
6. H.L. de Moraes, J. de Oliveira, Roberto eacute, D.C.R. Espinosa, oacute Ten, J.A.S. rio. Removal of iron from molten recycled aluminum through intermediate phase filtration. Mater. Trans., 47 (7) (2006) 1731-1736.
7. M. M.V. Fanconi, I. G. Fernández-Marcote, Í. Ruiz-Bustinza. The Challenge of Impurities (Fe, Si) to Recycling in the Rolled Aluminum Industry in the Coming

Years in Relation to Their Influence on Ultimate Tensile Strength. Metals, 13(12) (2023) 2014.
8. J. Lazaro-Nebreda, J. B. Patel, K. Al-Helal, F. Gao, I. Stone, G.M. Scamans, Z. Fan. De-Ironing of Aluminium Alloy Melts by High Shear Melt Conditioning Technology: An Overview. Metals, 12(10) (2022) 1579.
9. Y. Zhang, Y. Lei, Y. Ren, W. Ma. Removal of Fe impurities from Al alloy scraps by electromagnetic directional solidification combined with Si addition. J. Mater. Res. Technol. 26 (2023) 8737-8747.
10. R. Oliveira, R. Kakitani, L. R. Ramos, D. L. Gonçalves, A. Garcia, N. Cheung. The Roles of Mn and Ni Additions to Fe-Contaminated Al in Neutralizing Fe and Stabilizing the Cellular α-Al Microstructure. J. Sustain. Metall. 5 (2019) 561-580.
11. R. Kakitani, A.V. Rodrigues, C. Silva, A. Garcia, N. Cheung. The roles of solidification cooling rate and (Mn, Cr) alloying elements in the modification of β-AlFeSi and hardness evolvements in near-eutectic Al-Si alloys. J. Alloys Metall. Sys. 1 (2023) 100005.
12. Z. Que, Y. Wang, Z. Fan, T. Hashimoto, X.R. Zhou. Composition templating for heterogeneous nucleation of intermetallic compounds. Sci. Rep. 14 (2024) 8968.
13. K.M. Sree Manu, N. S. Barekar, J. Lazaro-Nebreda, J. B. Patel, Z. Fan. In-situ microstructural control of A6082 alloy to modify second phase particles by melt conditioned direct chill (MC-DC) casting process – A novel approach. J. Mater. Process. Tech. 295 (2021) 117170.
14. Z. Que, Y. Wang, C.L. Mendis, C. Fang, J. Xia, X. Zhou, Z. Fan. Understanding Fe-containing intermetallic compounds in Al alloys: An overview of recent advances from the LiME research hub. Metals 12 (10) (2022) 1677.
15. Z. Que, C. Fang, Z. Fan. Nucleation competition and phase transformation mechanisms in recycled aluminium alloys: Insights into θ-$Al_{13}Fe_4$, Al_6(Fe,Mn) and α-Al_{15}(Fe,Mn)$_3Si_2$. J. Alloys Comp. 1032 (2025) 181130.
16. S. Duan, M. Tang, W. Chen, C. Huang, J. Du. Microstructure evolution and mechanical properties of as-cast Al–Mg–Si alloy induced by Fe addition. J. Mater. Res. Tech. 39 (2025) 202-212.
17. Z. Que, C.L. Mendis. Formation of θ-$Al_{13}Fe_4$ and the multi-step phase transformations to α-Al_8Fe_2Si, β-Al_5FeSi and δ-Al_4FeSi_2 in Al–20Si-0.7 Fe alloy. Intermetallics 127 (2020) 106960.
18. H. Nowotny, R. Benesovsky. Über die Kristallstruktur von Al_6Fe, Zeitschrift für Metallkunde. 31 (1939) 222–225.
19. T. Turmezey, V. Stefániay, A. Griger. AlFeSi phases in Aluminium. Key Engineering Materials. 44-45 (1990) 57-68.
20. I. Butnariu, D. Butnariu, I. Butnariu. Studies and researches concerning the presence of iron in secondary aluminium meltings and valorification of some aluminium waste. Mater. Sci. Forum 690 (2011) 250-253.
21. Z. Fan, F. Gao, B. Jiang, Z. Que. Impeding Nucleation for More Significant Grain Refinement. Sci. Rep. 10 (2020) 9448.
22. E. Scheil. Bemerkungen zur Schichtkristallbildung. Z. Met. 34 (1942) 70-72.

23. Aluminium Association: Standard Test Procedure for Aluminium Alloy Grain Refiners: TP-1, Washington DC., 1987.
24. P. G. Enright, I. R. Hughes, J. Pickering, A. Simard, and J. Proulx. Characterisation of Molten Metal Quality Using the Pressure Filtration Technique. Trans. Am. Foundry Soc. (2003).
25. H. Men, Z. Fan. Prenucleation induced by crystalline substrates. Metall. Mater. Trans. A 49 (2018) 2766–2777.
26. Z. Fan. An Epitaxial Model for Heterogeneous Nucleation on Potent Substrates. Metall. Mater. Trans. A. 44 (2013) 1409-1418.
27. A.L. Geer, A. M. Bunn, A. Tronche, P. V. Evans, D. J. Bristow, Modelling of inoculation of metallic melts: Application to grain refinement of aluminium by Al–Ti–B. *Acta Mater.* 48(11) (2000) 2823–2835.
28. B. Jiang, H. Men, Z. Fan. Atomic ordering in the liquid adjacent to an atomically rough solid surface. Computational Materials Science, 153 (2018) 73-81.
29. M. L. Eastwood, S. Cremel, C. Gehrke, E. Girard, A.K. Bertram. Ice nucleation on mineral dust particles: Onset conditions, nucleation rates and contact angles. Geophys. Res. Atoms. 113 (D22) (2008).
30. S. L. Barr, B. Wyld, J.B. Mcquaid, R.R. Neely III, B.J. Murray. Southern Alaska as a source of atmospheric mineral dust and ice-nucleating particles. Sci. Adv. 9(33) (2023) 3708.
31. S.M. Liang, R. Schmid-Fetzer. Phosphorus in Al-Si cast alloys: thermodynamic prediction of the AlP and eutectic (Si) solidification sequence validated by microstructure and nucleation undercooling data. Acta Mater. 72 (2014) 41-56.
32. Z. Que, Y. Wang, Z. Fan, X. Zhou. Interfacial segregation of Fe and Si on TiB_2 surface and refinement of Fe-bearing intermetallic compounds and primary Si Part II Refinement of primary Fe-intermetallic compounds and primary Si through manipulating nucleation potency of TiB_2 particles. Mater. Sci. Eng. A 946 (2025) 149109.

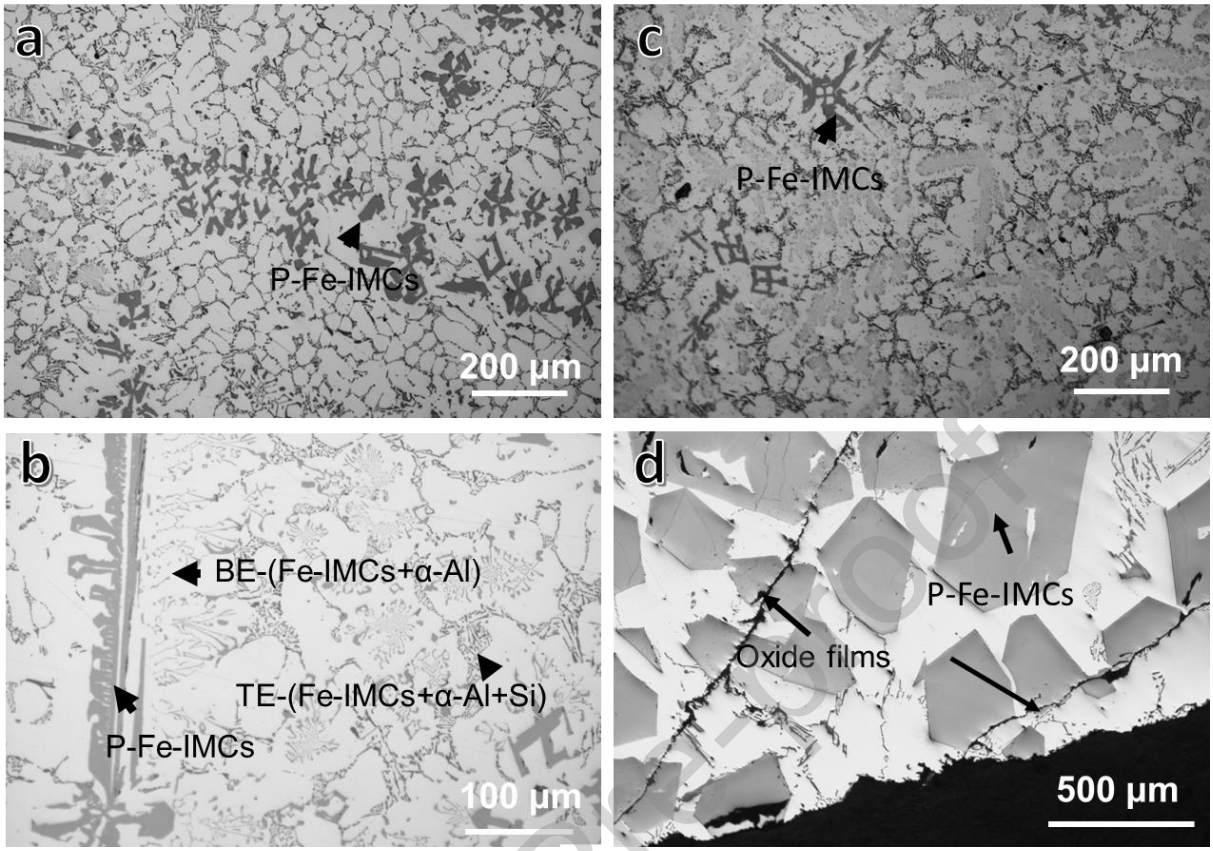

Figure 1. Optical micrographs of the as-cast Al-1.0Mn-2.2Fe-5Si alloy with pouring temperature of 750 ℃: (a) microstructure solidified at 3.5 K/s before pressure filtration; (b) higher magnification of image (a), showing binary and ternary eutectic structures; (c) microstructure solidified at 3.5 K/s cast from the melt after filtration, and (d) primary Fe-IMCs settled at the bottom of the crucible during slow cooling at 0.01 K/s.

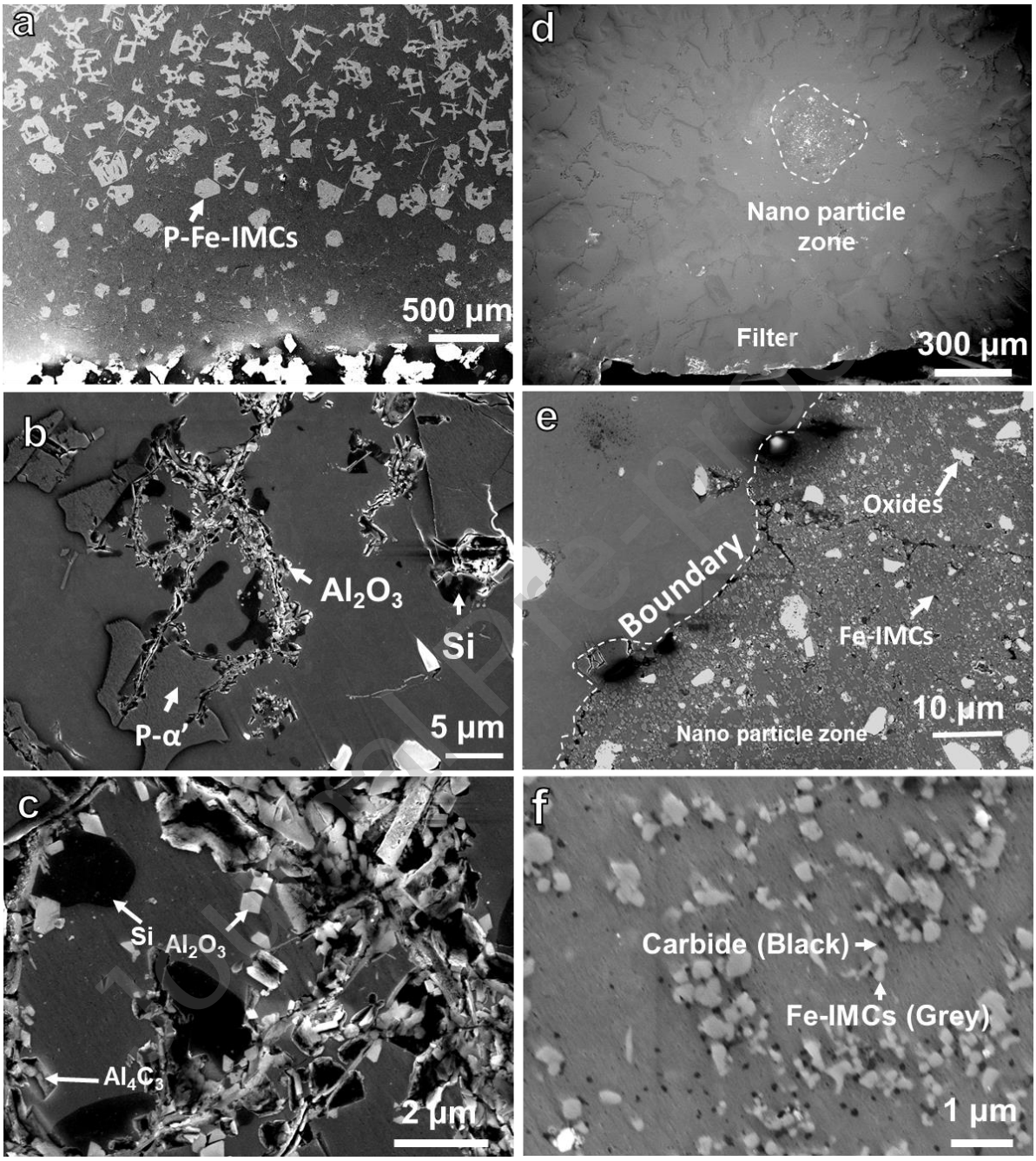

Figure 2. SEM images showing the pre-filtered microstructure of Al-1.0Mn-2.2Fe-5Si alloy: (a) primary Fe-IMC particles size increases with distance from the filter; (b) oxides collected above the filter; (c) collected inclusions mainly identified as Al_2O_3 and Al_4C_3; (d) region containing nano-particles above the filter; (e) boundary between the nano-particle zone and the matrix, where white particles are oxides observed using the in-lens detector, and (f) nano-sized Fe-IMCs associated with dark particles, observed in high - magnification SEM.

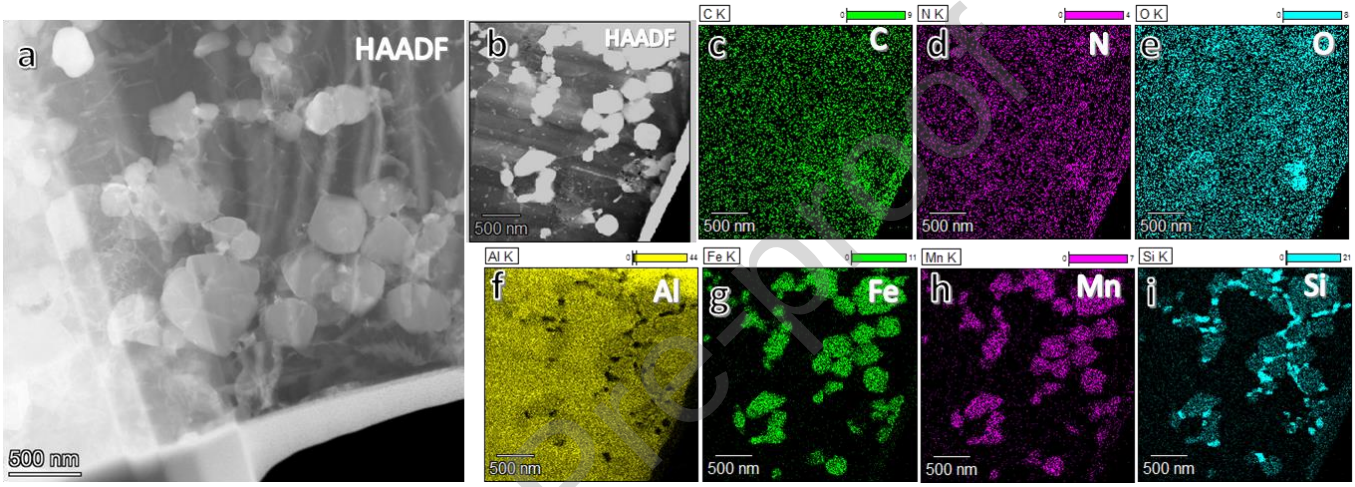

Figure 3. (a-b) HAADF - STEM images of the FIB lamella extracted from the oxide film area, showing particles ranging from a few tens to several hundred of nanometres in size; (c-i) STEM-EDS elemental maps of(c) C, (d) N, (e) O, (f) Al, (g) Fe, (h) Mn, (i) Si, revealing that most particles are Fe-IMC, along with some Si-rich particles embedded within the oxide films.

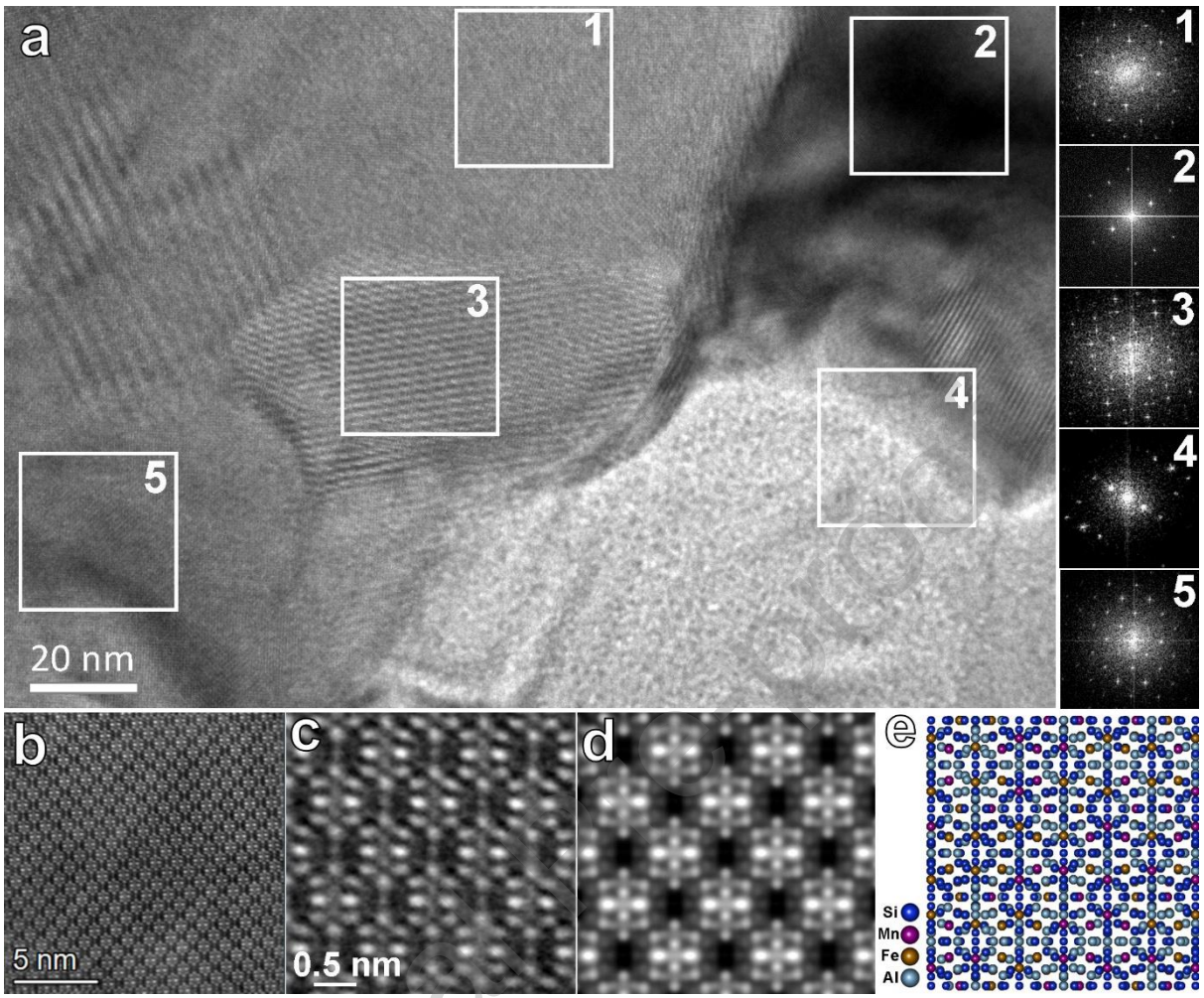

Figure 4. (a) HAADF – STEM image of a single Fe-IMC particle and corresponding FFT patterns from different positions, revealing nanoscale defects and local phase transitions that complicate crystallographic phase identification; (b) experimental atomic resolution HAADF-STEM image of α-$Al_{15}(Fe,Mn)_3Si_2$ viewed along [100] zone axis; (c) magnified view of an area from experimental image b; (d) simulated HAADF-STEM image and (e) corresponding atomic model of α-$Al_{15}(Fe,Mn)_3Si_2$ along the [100] zone axis.

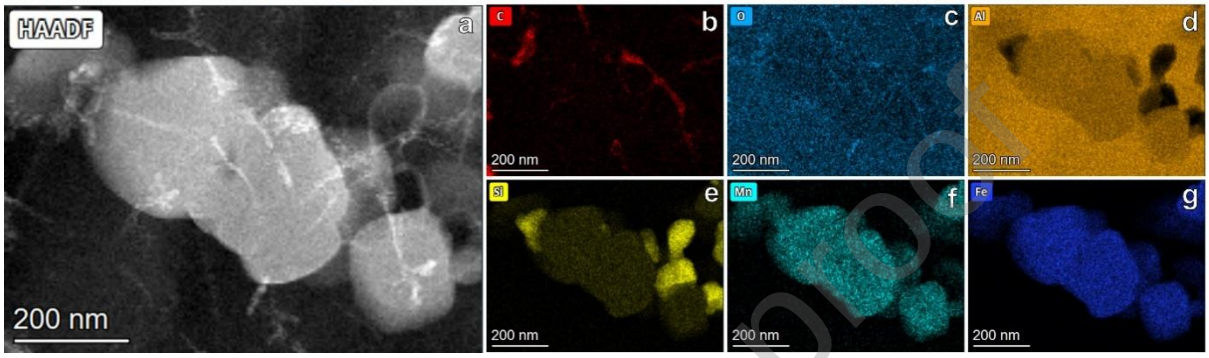

Figure 5. (a) HAADF-STEM image, and corresponding STEM-EDS elemental maps: (b) C, (c) O, (d) Al, (e) Si, (f) Mn and (g) Fe, revealing oxide films embedded within the Fe-IMC particles and Si particles connected to these Fe-IMCs.

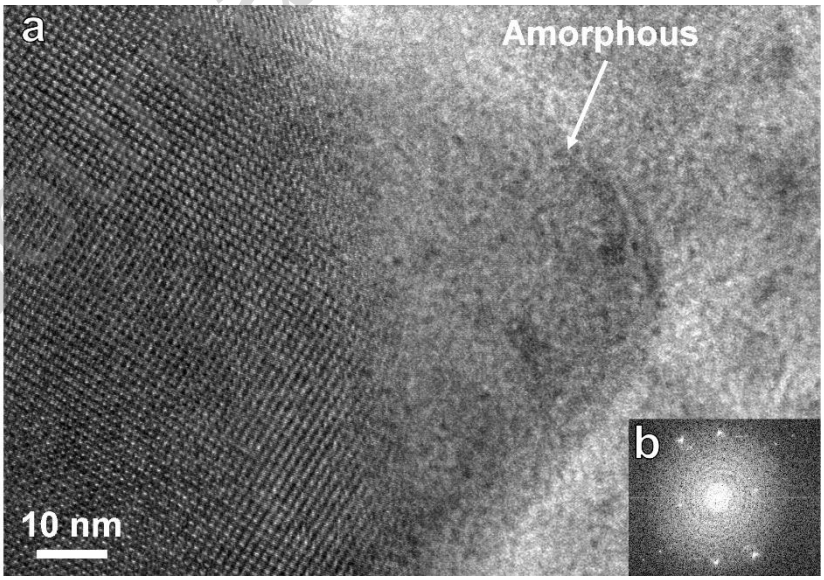

Figure 6. (a) HAADF-STEM image showing a Fe-IMC particle associated with an amorphous oxide; (b) FFT pattern from the oxide region, confirming its amorphous nature.

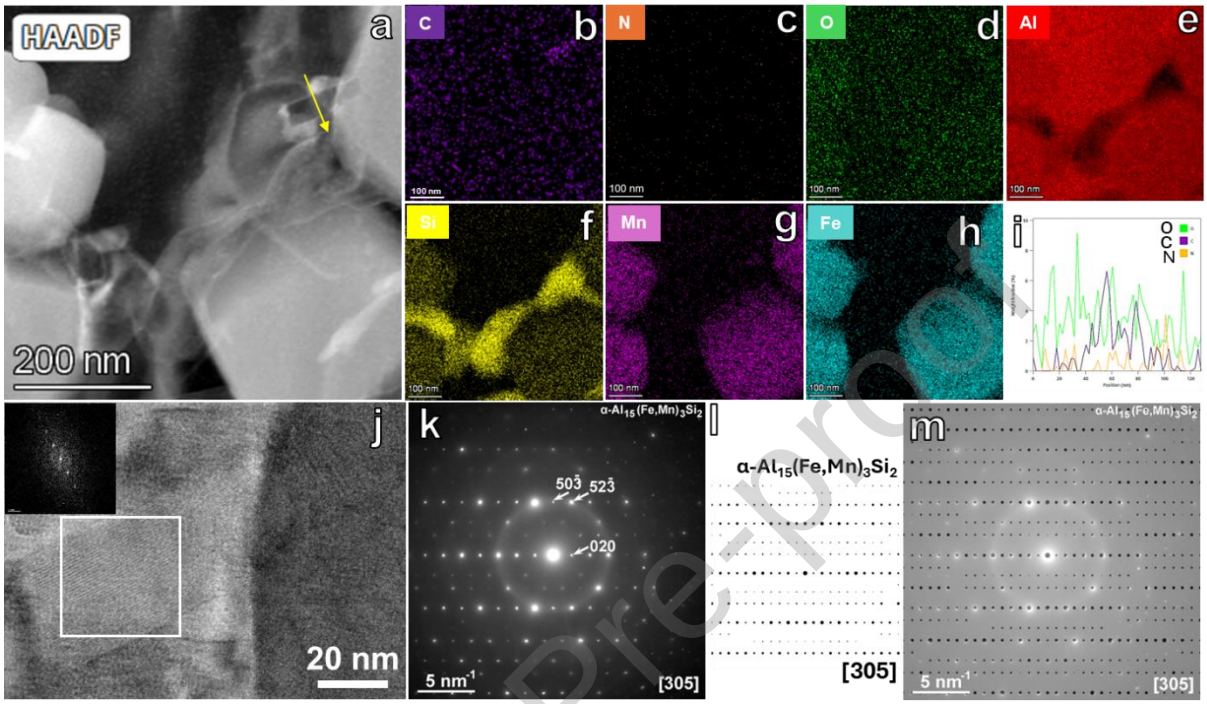

Figure 7. (a) HAADF-STEM image showing Fe-IMC particles associated with elongated, needle-like dark inclusions; (b–h) STEM-EDS elemental maps indicating that this needle-like structure is C-rich; (i) intensity profile extracted from STEM-EDS mapping (a) along yellow arrow, confirming carbon enrichment of the inclusion; (j) HRTEM image highlighting crystallographic features of the needle, although the FFT does not indicate clear crystallization; (k) experimental and (l) corresponding simulated SAED pattern of α-$Al_{15}(Fe,Mn)_3Si_2$ along the [305] zone axis; (m) superposition of the experimental (k) and simulated (l) SAED patterns demonstrates that the Fe-IMC particle is structurally consistent with α-$Al_{15}(Fe,Mn)_3Si_2$ and is associated with the adjacent carbon-rich inclusion.

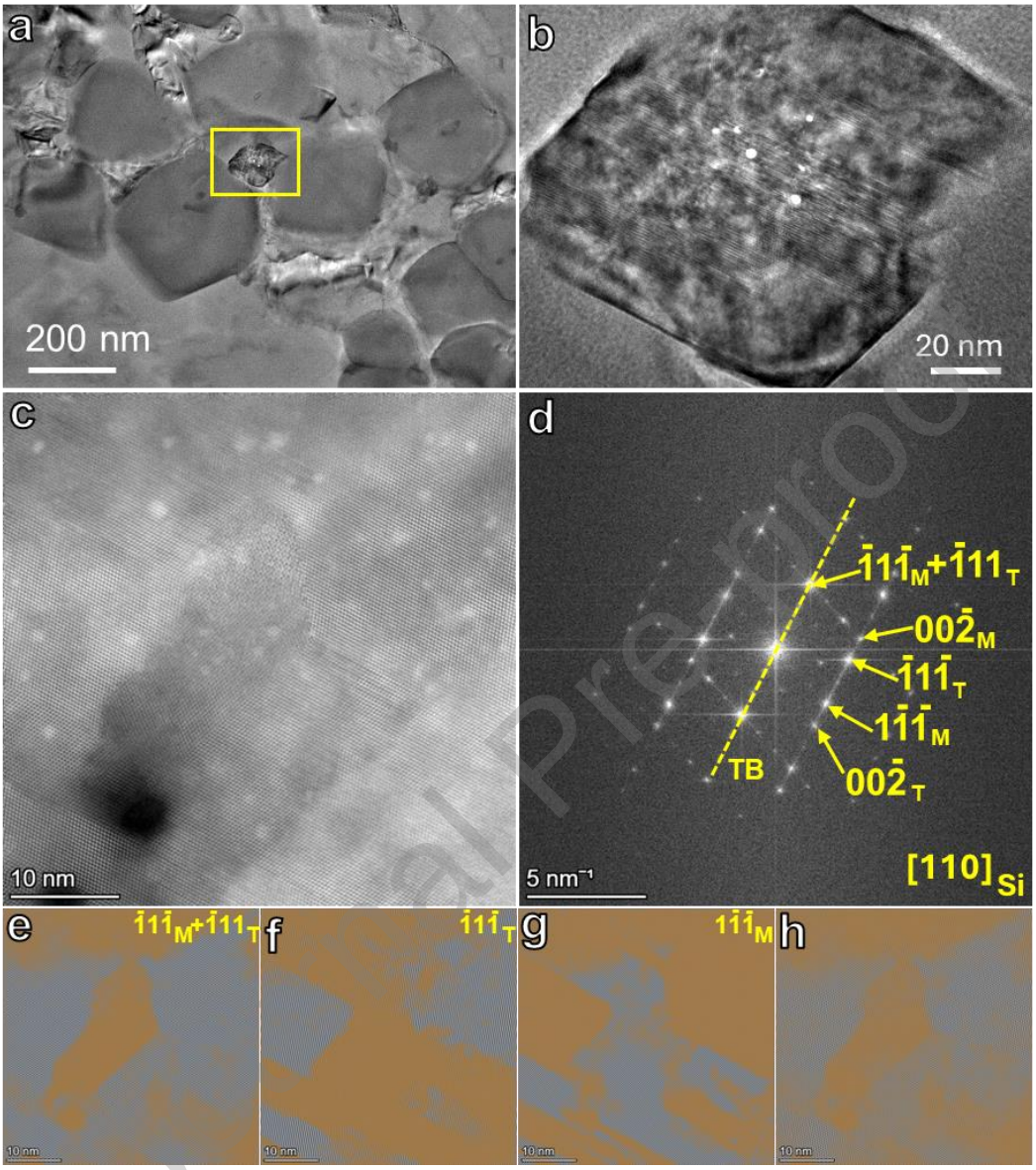

Figure 8. (a) Bright field (BF)-TEM image showing a nanoscale Si particle between Fe-IMC particles; (b) HRTEM image revealing the complex twinning structure of the Si particle; (c) HAADF-STEM image highlighting the twinning features and a central overlap region; (d) corresponding indexed FFT pattern confirming twinning along the {111} planes; (e-g) filtered FFT images of the STEM image (c), obtained from the indicated spots; (h) filtered FFT image generated by combining three spots, $\bar{1}1\bar{1}_M+\bar{1}11_T$, $\bar{1}1\bar{1}_T$ and $1\bar{1}\bar{1}_M$, showing that the central core corresponds to overlapping twinning planes rather than a distinct phase. Note: T represents the twin plane, while M represents the matrix.

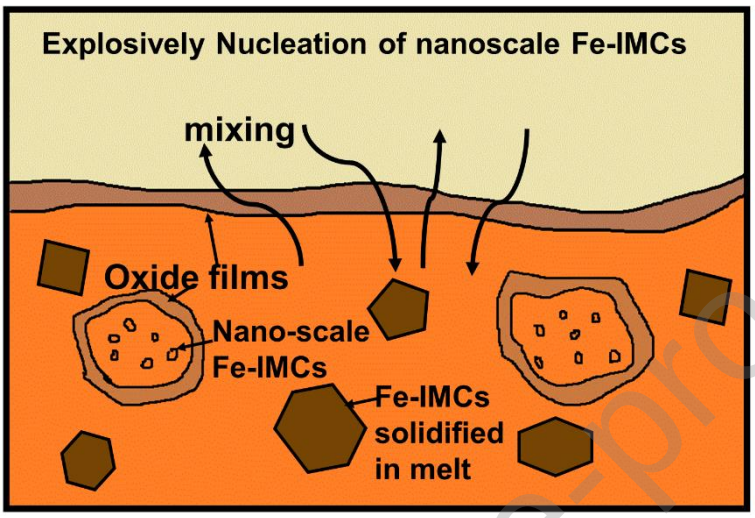

Figure 9. Schematic illustration of oxide films formation and their role in trapping liquid alloy, leading to the formation of localized, confined bulk melt regions. Natural formation of oxide films on the surface of molten Al, and confinement of alloy melt within oxide films due to stirring or mixing, followed by rapid oxide formation that encloses the melt within the film.

Table 1. Composition of the Fe-IMCs in this study

at.%	Al	Fe	Mn	Si	Analysis way
Fe-IMCs in TP-1 sample	75.12±5.9	11.17±2.1	5.79±1.1	7.92±1.9	SEM-EDS (>20 particles)
Fe-IMCs in prefilled sample	75.1±5.7	11.1±2.5	5.8±1.0	8.0±2.1	SEM-EDS (>20 particles)
Fe-IMC in Nano zone	70.8±4.6	14.79±1.4	5.56±0.8	8.81±1.7	TEM-EDS (>20 particles)

Graphical abstract

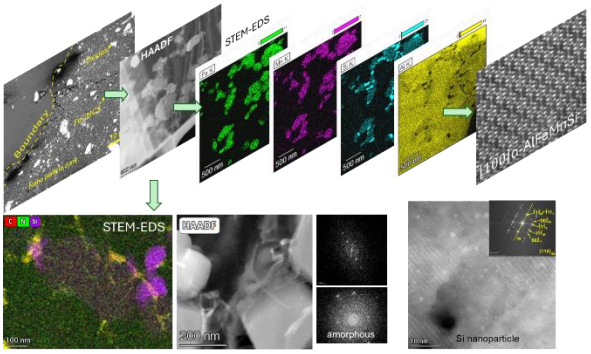

Declaration of interests

☐ The authors declare that they have no known competing financial interests or personal relationships that could have appeared to influence the work reported in this paper.

☒ The authors declare the following financial interests/personal relationships which may be considered as potential competing interests:

Zhongyun Fan reports financial support was provided by Engineering and Physical Sciences Research Council. If there are other authors, they declare that they have no known competing financial interests or personal relationships that could have appeared to influence the work reported in this paper.

Highlights

- High density of nanoscale α-$Al_{15}(Fe,Mn)_3Si_2$ particles were solidified within confined oxide films in an Al-1Mn-2.2Fe-5Si alloy.
- The oxides and inclusions within this confined oxide film are amorphous.
- The Si phase, which is as difficult to nucleate as Fe-IMCs, was also refined to the nanoscale within this confined melt.